Supporting Information

New Solid Electrolyte $Na_9Al(MoO_4)_6$: Structure and Na^+ Ion Conductivity

Aleksandra A. Savina, Vladimir A. Morozov, Anton L. Buzlukov, Irina Yu. Arapova, Sergey Yu. Stefanovich, Yana V. Baklanova, Tatiana A. Denisova, Nadezhda I. Medvedeva, Michel Bardet, Joke Hadermann, Bogdan I. Lazoryak, Elena G. Khaikina

Table S1. Atomic coordinates and equivalent isotropic displacement parameters for $Na_9Al(MoO_4)_6$.

	R-3*c*	*R*-3	*C*2/*c*
Al			
site symmetry	6*a*	6*c*	4*e*
g_i, *occupancy*	1	1	1
x/a	0	0	0
y/b	0	0	0.255(4)
z/c	0.25	0.2580(15)	0.25
U_{iso}*/U_{eq}	0.017(3)	0.006(4)	0.001(4)
Na1			
site symmetry	18*e*	18*f*	4*e*
g_i, *occupancy*	1	1	1
x/a	0.7774(	-0.0084(15)	0
y/b	0	0.2196(9)	0.035(3)
z/c	0.25	0.2621(9)	0.25
U_{iso}*/U_{eq}	0.051(3)	0.0281(19)	0.018(2)
Na2			
site symmetry	36*f*	18*f*	8*f*
g_i, *occupancy*	1	1	1
x/a	0.5618(4)	0.0038(17)	0.6260(19)
y/b	0.6688(4)	0.2301(17)	0.858(2)
z/c	0.2171(3)	0.0529(12)	0.469(3)
U_{iso}*/U_{eq}	0.036(2)	0.0281(19)	0.018(2)
Na3			
site symmetry		18*f*	8*f*
g_i, *occupancy*		1	1
x/a		0.0061(17)	0.306(2)
y/b		0.2296(16)	0.525(2)
z/c		0.4506(12)	0.469(3)
U_{iso}*/U_{eq}		0.0281(19)	0.018(2)
Na4			
site symmetry			8*f*
g_i, *occupancy*			1
x/a			0.421(2)
y/b			0.858(2)

z/c			0.678(3)
U_{iso}*/U_{eq}			0.018(2)
Na5			
site symmetry			8*f*
g_i, *occupancy*			1
x/a			0.688(3)
y/b			0.368(3)
z/c			0.221(3)
U_{iso}*/U_{eq}			0.018(2)
Mo1			
site symmetry	36*f*	18*f*	8*f*
g_i, *occupancy*	1	1	1
x/a	0.51807(9)	0.5205(5)	0.5135(6)
y/b	0.66012(11)	0.8570(4)	0.6487(6)
z/c	0.02360(6)	0.0241(3)	0.9592(8)
U_{iso}*/U_{eq}	0.0117(4)	0.0122(4)	0.0028(4)
Mo2			
site symmetry		18*f*	8*f*
g_i, *occupancy*		1	1
x/a		0.5160(4)	0.7003(6)
y/b		0.6570(4)	0.6562(6)
z/c		0.5230(3)	0.3279(7)
U_{iso}*/U_{eq}		0.0122(4)	0.0028(4)
Mo3			
site symmetry			8*f*
g_i, *occupancy*			1
x/a			0.6007(6)
y/b			0.9393(6)
z/c			0.1334(9)
U_{iso}*/U_{eq}			0.0028(4)
O1			
site symmetry	36*f*	18*f*	8*f*
g_i, *occupancy*	1	1	1
x/a	0.2750(6)	0.5740(18)	0.489(3)
y/b	0.7314(6)	0.7800(19)	0.755(2)
z/c	0.8560(3)	0.0270(13)	0.890(4)
U_{iso}*/U_{eq}	0.033(3)	0.0131(19)	0.0008(20)
O2			
site symmetry	36*f*	18*f*	8*f*
g_i, *occupancy*	1	1	1
x/a	0.4817(6)	0.4926(15)	0.621(2)
y/b	0.6088(6)	0.8888(15)	0.618(3)
z/c	0.1120(4)	0.1084(11)	0.907(3)
U_{iso}*/U_{eq}	0.038(3)	0.0131(19)	0.0008(20)
O3			
site symmetry	36*f*	18*f*	8*f*
g_i, *occupancy*	1	1	1

x/a	0.0454(6)	0.6161(17)	0.435(3)
y/b	0.7283(6)	0.9806(19)	0.582(3)
z/c	0.8224(4)	-0.0070(10)	0.887(4)
U_{iso}*/U_{eq}	0.031(3)	0.0131(19)	0.0008(20)
O4			
site symmetry	36*f*	18*f*	8*f*
g_i, *occupancy*	1	1	1
x/a	0.0798(6)	0.3998(17)	0.540(2)
y/b	0.5446(5)	0.8091(15)	0.657(3)
z/c	0.8081(3)	-0.0188(11)	0.135(3)
U_{iso}*/U_{eq}	0.012(3)	0.0131(19)	0.0008(20)
O5			
site symmetry		18*f*	8*f*
g_i, *occupancy*		1	1
x/a		0.6007(17)	0.659(2)
y/b		0.8012(19)	0.548(2)
z/c		0.5217(12)	0.268(3)
U_{iso}*/U_{eq}		0.0131(19)	0.0008(20)
O6			
site symmetry		18*f*	8*f*
g_i, *occupancy*		1	1
x/a		0.4706(15)	0.801(2)
y/b		0.6146(19)	0.711(2)
z/c		0.6159(11)	0.287(4)
U_{iso}*/U_{eq}		0.0131(19)	0.0008(20)
O7			
site symmetry		18*f*	8*f*
g_i, *occupancy*		1	1
x/a		0.5888(19)	0.728(2)
y/b		0.6030(17)	0.6672(17)
z/c		0.4842(13)	0.498(3)
U_{iso}*/U_{eq}		0.002(3)	0.0008(20)
O8			
site symmetry		18*f*	8*f*
g_i, *occupancy*		1	1
x/a		0.5921(17)	0.613(2)
y/b		0.6045(14)	0.736(2)
z/c		0.4851(11)	0.306(4)
U_{iso}*/U_{eq}		0.0131(19)	0.0008(20)
O9			
site symmetry			8*f*
g_i, *occupancy*			1
x/a			0.674(2)
y/b			0.938(2)
z/c			0.273(4)
U_{iso}*/U_{eq}			0.0008(20)
O10			
site symmetry			8*f*

g_i, *occupancy*			1
x/a			0.6833(18)
y/b			0.912(2)
z/c			1.010(3)
U_{iso}*/U_{eq}			0.0008(20)
O11			
site symmetry			8*f*
g_i, *occupancy*			1
x/a			0.547(3)
y/b			0.054(2)
z/c			0.143(4)
U_{iso}*/U_{eq}			0.0008(20)
O12			
site symmetry			8*f*
g_i, *occupancy*			1
x/a			0.523(3)
y/b			0.848(3)
z/c			0.126(5)
U_{iso}*/U_{eq}			0.0008(20)

Table S2. Bond lengths (Å) and angles (°) for $Na_9Al(MoO_4)_6$.

	R-3*c*		*R*-3		*C*2/*c*
AlO_6- *octahedron*					
Al-O4×6	1.951(9)	Al-O4×3	2.11(3)	Al-O4×2	2.02(6)
		Al-O8×3	1.88(3)	Al-O8×2	1.83(4)
				Al-O12×2	1.93(6)
		<Al-O>	1.995	<Al-O>	1.927
$Na1O_6$- *polyhedron*					
Na1-O1×2	2.403(10)	Na1-O1	2.39(3)	Na1-O3×2	2.51(5)
Na1-O3×2	2.431(10)	Na1-O3	2.27(3)	Na1-O4×2	2.27(6)
Na1-O4×2	2.643(7)	Na1-O4	2.18(3)	Na1-O5×2	2.45(4)
		Na1-O5	2.91(3)		
		Na1-O7	2.60(3)		
		Na1-O8	2.63(3)		
<Na1-O>	2.492	<Na1-O>	2.497	<Na1-O>	2.410 (10.6)
$Na2O_6$- *polyhedron*					
Na2-O2	2.288(10)	Na2-O1	2.96(3)	Na2-O1	2.83(5)
Na2-O2	2.323(14)	Na2-O3	2.33(5)	Na2-O7	2.28(4)
Na2-O3	2.462(11)	Na2-O5	2.45(4)	Na2-O8	2.50(5)
Na2-O4	2.548(10)	Na2-O6	2.30(4)	Na2-O9	2.55(3)
Na2-O4	2.911(14)	Na2-O6	2.38(3)	Na2-O11	2.61(5)
Na2-O4	2.415(8)	Na2-O7	2.45(4)	Na2-O12	2.45(5)
<Na2-O>	2.491	<Na2-O>	2.478	<Na2-O>	2.537(24.1)
$Na3O_6$- *polyhedron*					
		Na3-O1	2.39(3)	Na3-O2	2.15(3)
		Na3-O2	2.31(4)	Na3-O3	2.72(5)
		Na3-O2	2.32(3)	Na3-O5	2.63(5)
		Na3-O3	2.65(3)	Na3-O5	3.01(5)
		Na3-O5	2.86(4)	Na3-O7	2.89(4)
		Na3-O7	2.65(4)	Na3-O10	2.17(4)
		<Na3-O>	2.530	<Na3-O>	2.595
$Na4O_6$- *polyhedron*					
				Na4-O1	2.85(5)
				Na4-O1	2.21(5)
				Na4-O6	2.46(5)
				Na4-O10	2.60(4)
				Na4-O11	2.32(5)
				Na4-O11	2.38(5)
				<Na4-O>	2.470(29.0)
$Na5O_6$- *polyhedron*					
				Na5-O2	2.30(4)
				Na5-O3	2.26(6)
				Na5-O5	2.73(5)
				Na5-O6	2.31(5)
				Na5-O7	2.54(5)
				Na5-O9	2.36(4)
				<Na5-O>	2.417(20.8)
$Mo1O_4$- *tetrahedron*					
Mo1-O1	1.769(8)	Mo1-O1	1.67(3)	Mo1-O1	1.75(4)
Mo1-O2	1.833(8)	Mo1-O2	1.80(2)	Mo1-O2	1.84(4)
Mo1-O3	1.766(10)	Mo1-O3	1.75(2)	Mo1-O3	1.70(4)
Mo1-O4	1.751(10)	Mo1-O4	1.75(2)	Mo1-O4	1.88(4)
<Mo1-O>	1.780	<Mo1-O>	1.743	<Mo1-O>	1.793
$Mo2O_4$- *tetrahedron*					

		Mo2-O5	1.84(2)	Mo2-O5	1.80(3)
		Mo2-O6	1.91(2)	Mo2-O6	1.83(3)
		Mo2-O7	1.80(3)	Mo2-O7	1.84(3)
		Mo2-O8	1.80(2)	Mo2-O8	1.74(4)
		<Mo2-O>	1.838	<Mo2-O>	1.803
$Mo3O_4$- *tetrahedron*					
				Mo3-O3	1.80(3)
				Mo3-O6	1.93(3)
				Mo3-O9	1.88(4)
				Mo3-O12	1.80(4)
				<Mo3-O>	1.853

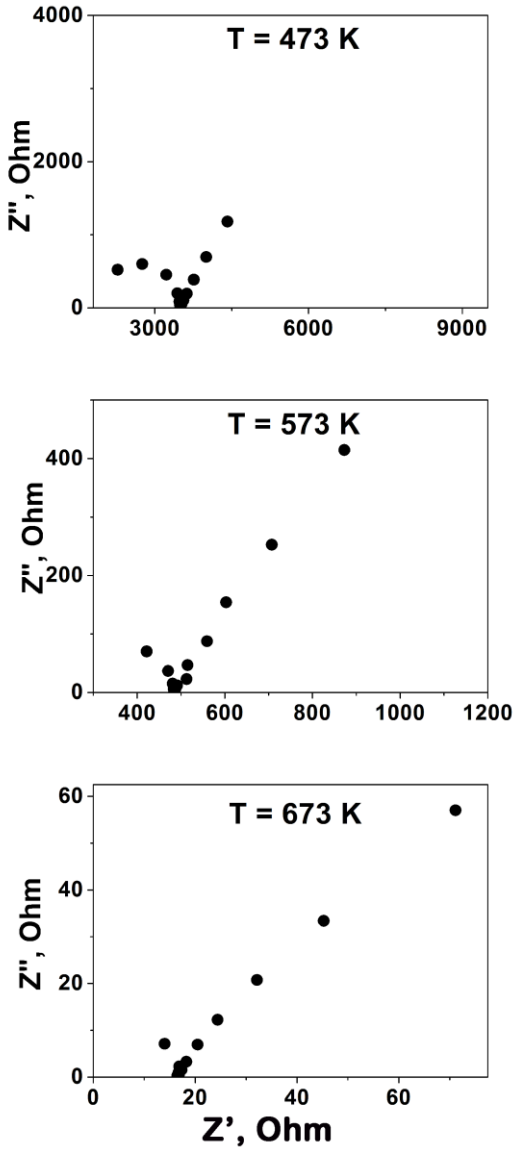

Figure S1. Impedance spectra of $Na_9Al(MoO_4)_6$ at different temperatures

^{23}Na NMR at room temperature: assignment of different spectral components to the distinct positions of Na^+ ions in the $Na_9Al(MoO_4)_6$

Figure S2 shows the ^{23}Na NMR spectral lines obtained in external magnetic fields of 11.7 T (Larmor frequency ^{23}Na, $\omega_0/2\pi$ = 132.29 MHz) and 4.7 T ($\omega_0/2\pi$ = 52.94 MHz). Similar NMR spectra were also obtained in the 9.4 T magnetic field ($\omega_0/2\pi$ = 105.82 MHz, not shown here).

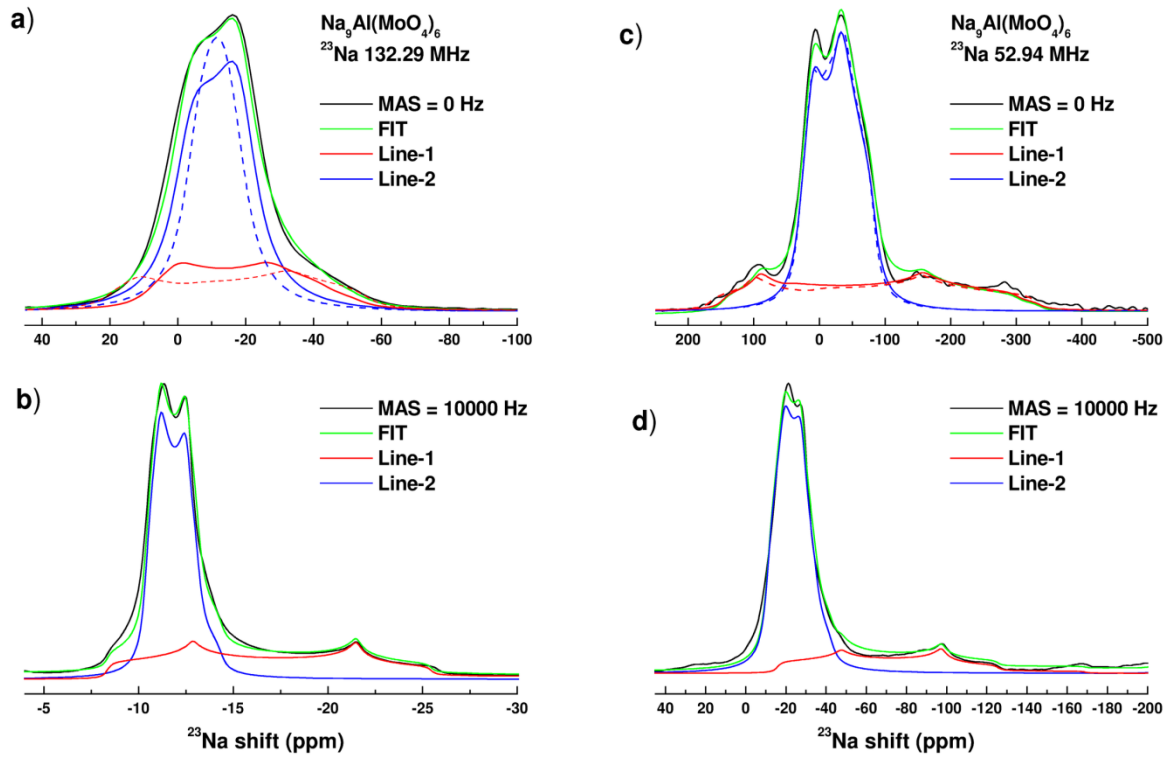

Figure S2. ^{23}Na NMR spectra obtained in magnetic fields 11.7 T (a, b) and 4.7 T (c, d) in static and MAS regimes. The color lines represent the results of the approximation of the spectra in various models (see text).

As can be seen from the presented data, a decrease of the external magnetic field intensity leads to a substantial broadening of the NMR spectrum. Similar effects can be expected only in one case, namely, when the main factor determining the form of the NMR spectrum is the quadrupole interaction. Nuclei with a spin quantum number $I > 1/2$ have a non-spherical charge distribution in the nucleus. This leads to the appearance of a quadrupole moment that interacts with the Electric Field Gradient (EFG) present on the nucleus. The components of the EFG tensor are determined, in their turn, by the features of the local environment [1]. In the case of strong magnetic fields, the influence of the quadrupole interaction is usually described as small corrections to the Zeeman energy within the framework of perturbation theory. In the first order of perturbation theory, the presence of a quadrupole interaction leads to a characteristic splitting

of NMR spectrum and to appearance (in the case of ^{23}Na with I = 3/2) of three lines: the line corresponding to the central transition, $m_I = -1/2 \leftrightarrow +1/2$, and two satellite lines ($m_I = \pm 3/2 \leftrightarrow \pm 1/2$). For a powder sample, the peaks of satellites are shifted relative to the position of the central line by a distance of $\pm 1/2 \nu_Q(1 - \eta)$, where the values of the quadrupole frequency, ν_Q, and the asymmetry parameter, η, are determined by the components of the EFG tensor: $\nu_Q \equiv \omega_Q/2\pi = (3eQ/2I(2I - 1)h)V_{ZZ}$; $\eta = (V_{XX} - V_{YY})/V_{ZZ}$. At sufficiently high values of the EFG, an important role is played also by second-order effects, which are manifested in the characteristic splitting of the central line. The splitting value it is inversely proportional to the resonant frequency.[2]

All MAS spectra and static spectrum recorded in a weak magnetic field can be described as a superposition of two lines with significantly different parameters ν_Q = 1370 ± 50 and 600 ± 50 kHz; and η = 0.3–0.4 and 0.5–0.7 for Line-1 (red in Figure S2) and Line-2 (blue), respectively. Relative intensities of the corresponding NMR signals, $^{(1)}I \approx 0.35$ and $^{(2)}I \approx 0.65$. It should be noted, however, that for the static spectrum acquired in a more intense external magnetic field, this model taking into account only the second-order quadrupolar effects is clearly insufficient (the dashed lines in Figure S2a). Interestingly that, the splitting of Line-2 is certainly not enough, while for Line-1 it is is redundant (for any reasonable spectrum deconvolution the values ν_Q < 1200 kHz and ν_Q > 800 kHz are required for Line-1 and Line-2, respectively). Thus, the shape of the ^{23}Na NMR spectrum in the $Na_9Al(MoO_4)_6$ is obviously determined not only by quadrupole, but also by other type of interaction depending on the intensity of external magnetic field. This interaction has to be weak enough to be averaged already at MAS = 10 kHz. Moreover this additional contribution must have the different “directions" for Lines 1 and 2. The most probable candidate for such an additional interaction in the case of $Na_9Al(MoO_4)_6$ is the dipolar interaction between ^{23}Na nuclei and unpaired electrons (most likely the 4*d* of Mo^{6+}). In the DMFit program [3], the electron-nuclear dipolar interaction can be accounted for by introducing an additional parameter: chemical shift anisotropy (CSA). The parameters of the anisotropy and asymmetry of the chemical shift tensor are determined by the corresponding components: $\Delta\delta = \delta_{33} - \delta_{iso}$, $\eta_{CS} = |\delta_{22} - \delta_{11}|/|\delta_{33} - \delta_{iso}|$, where the isotropic shift, $\delta_{iso} = (\delta_{11} + \delta_{22} + \delta_{33})/3$ [4,5]. It can be seen that the $\Delta\delta$ value can have a different sign (depending on the local atomic configuration). In addition, the greatest effect can be expected in high magnetic field, since it is directly determined by the average magnetic moment of the electrons, i.e. it is proportional to the sample magnetization (see, for example, [6]). As can be seen for Figure S2 (solid lines) the model "EFG 2nd+CSA" allows to describe satisfactorily all spectral lines irrespective of the external magnetic field intensity and regardless of the spectrum measuring technique (static or MAS mode). The values of $\Delta\delta$ are approximately 2500 and – 900 Hz for lines 1 and 2, respectively. The η_{CS} value is close to zero for both lines. As it was found previously [7] in the related solid solutions

$Sc_2(W_xMo_{1-x}O_4)_3$, on the ^{17}O nuclei the value of $\Delta\delta \sim 20$ kHz . Thus, our estimates of $\Delta\delta$ seem to be quite reasonable, taking into account the distances typical for these structures (1.7–1.9 Å for Mo–O, and 3.5–4.4 Å for Mo–Na).

NMR experiments together with the DFT calculations allow us to attribute the two detected NMR signals to distinct structural positions of Na^+ ions in the $Na_9Al(MoO_4)_6$ oxide. As noted in Section 3.6 the compound structure assumes the filling of five types of crystallographic positions with a highly distorted octahedral anionic environment: Na1 and Na2 ions that are placed in the vicinity of AlO_6 octahedra, and Na3–Na5 ions which are located in the cavities of the $[Al(MoO_4)_6]^{-9}$ clusters framework. We assign the detected Line-1 to the positions Na1–Na2, and Line-2 to the Na3–Na5 ions, respectively. This conclusion is confirmed first by comparing the relative intensities of the corresponding signals ($^{(1)}I \approx 0.35$, $^{(2)}I \approx 0.65$), which agrees perfectly well with the filling factors of the corresponding positions. Moreover, this conclusion coincides qualitatively with the results of DFT calculations (see Table S3). The calculated nuclear quadrupole interaction parameters with and without structural optimization are listed in Table S1, where we used the quadrupole moments of 104 b and 146.6 b for ^{23}Na and ^{27}Al nuclei, respectively. Without structural optimization, the five distinct Na sites in *C*2/*c* have the very different magnitudes and signs of EFG, and the η values are varied strongly from 0.1 to 0.99 (Table S3). Structural optimization of atomic coordinates in *C*2/*c* leads to the only two sets of ν_Q (1.85 and -0.73 MHz) and η (0.36 and 0.69). It has to be noted that in the experimental NMR studies there is an ambiguity in the sign of EFG and only its magnitude is determined.

It can be seen that although the values ν_Q and η obtained in the *ab-initio* calculations slightly exceed the estimates based on NMR data, nevertheless, there is a clear tendency to "segregation" into two types of EFG parameters corresponding to Na1–Na2 and Na3–Na5. Another (although indirect) confirmation is the temperature behavior of the ^{27}Al NMR signal parameters (see Section 3.7).

Table S3. Quadrupole frequencies ν_Q (MHz) and asymmetry parameters η at ^{23}Na and ^{27}Al nuclei calculated for experimental and optimized atomic coordinates in *C*2/*c* $Na_9Al(MoO_4)_6$

	Experimental structure		Optimized structure	
Na site	ν_Q	η	ν_Q	η
Na1*4	2.02	0.20	1.92	0.35
Na2*8	-1.65	0.82	1.92	0.35
Na3*8	2.14	0.13	-0.76	0.69
Na4*8	1.26	0.99	-0.76	0.69
Na5*8	-0.84	0.17	-0.76	0.69
Al	-0.20	0.10	0.15	0.10

Second moment of the NMR line

Second moment of the NMR line which is known to be determined by Van Vleck's expression[8]:

$$\left\langle \Delta\omega^2 \right\rangle = \left\langle \Delta\omega_{II}^2 \right\rangle + \left\langle \Delta\omega_{IS}^2 \right\rangle = \frac{3}{5}\gamma_I^4\hbar^2 I(I+1)\sum_j r_{ij}^{-6} + \frac{4}{15}\gamma_I^2\gamma_S^2\hbar^2 S(S+1)\sum_k r_{ik}^{-6}, \qquad (1)$$

where the first term takes into account the dipolar interaction between identical spins (Na–Na in our case), and the second term between the different spins (Na–Al). The values γ_I and γ_S are the gyromagnetic ratios of the corresponding nuclei, I and S their spin values (3/2 for ^{23}Na and 5/2 for ^{27}Al), and the $r_{ij(k)}$ the distance between the interacting nuclei.

Spin-lattice relaxation rate of the ^{23}Na

Measurements of the ^{23}Na spin-lattice relaxation rates, T_1^{-1}, have been performed in the temperature range 300–750 K, in a magnetic field 11.7 T. For the entire temperature range, the recovery of the nuclear magnetization after the inverting pulse was characterized by nonexponential behavior (see Inset in Figure S3 for an illustration). At least two components of the relaxation rate were required for the experimental data fit: $M_z(t) = M_{z,eq} - [M_{z,eq} - M_z(0)](c_s\exp(-t/T_{1S}) + c_f\exp(-t/T_{1F}))$, where $M_{z,eq}$ is the equilibrium value of the nuclear magnetization, T_{1F} и T_{1S} are the fast and slow components of the spin-lattice relaxation, respectively, and c_s and c_f determine the fractions of the corresponding components ($c_s + c_f = 1$).

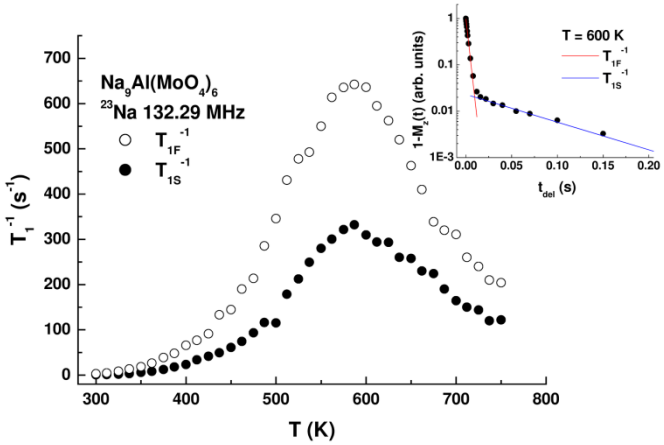

Figure S3. The temperature dependencies of the fast and slow spin-lattice relaxation components of ^{23}Na nuclei measured for the $Na_9Al(MoO_4)_6$ compound in the temperature range 300–750 K. Inset shows an example of the nuclear magnetization recovery acquired at T = 600 K. The red and blue lines are given as the eyesguides for representation of fast and slow components of the spin-lattice relaxation rate.

For the entire temperature range, the value of c_s = 0.6±0.1. On the one hand, the appearance of two "branches" of the spin-lattice relaxation for ^{23}Na nuclei (with I = 3/2) can be

expected due to quadrupole relaxation mechanisms (see, for example, [9, 10]). The values c_s and c_f found in our experiments are close to those expected in the case of excitation and detection of only the central transition: $c_s = c_f = 0.5$ [11]. On the other hand, the observed values $c_s \approx 0.6$, $c_f \approx 0.4$ are close to the relative intensities for Line-2 and Line-1. This could allow, in principle, to assign the two branches of the spin-lattice relaxation T_{1S}^{-1} and T_{1F}^{-1} directly to the observed NMR signals. Indeed, in some cases [12–16], it was possible to attribute different components of the relaxation rate to distinct spectral components. However, these results were obtained for the ^{7}Li nuclei. As was noted in [17–19], the emergence of the mono-exponential character of the nuclear magnetization recovery should be expected for the cases when flip-flop dipolar interaction between the pairs of spins is comparable with the quadrupolar interactions inducing the spin-lattice relaxation. The ^{7}Li nuclei are characterized by a high value of the gyromagnetic ratio (which assumes the strong homonuclear dipolar interaction) and, at the same time, rather low ν_Q values (which do not exceed, usually, hundred kHz). In this case the quadrupole effects in the M_z recovery indeed can be "smoothed out " due to spin/atomic diffusion. In our case, the opposite situation is observed: a lower value of $^{23}\gamma$ and substantially higher values of ν_Q: ≈ 1350 and 600 kHz for lines 1 and 2, respectively. Thus, we assume that the ^{23}Na spin-lattice relaxation in the $Na_9Al(MoO_4)_6$ is determined mainly by quadrupole mechanisms (as it is shown in Section 3.8 the dipolar contribution to T_1^{-1} can be completely neglected), and the appearance of the nonexponential $M_z(t)$ behavior is exclusively due to this. Figure S3 presents the temperature dependencies of T_{1F}^{-1} and T_{1S}^{-1} for ^{23}Na nuclei in the $Na_9Al(MoO_4)_6$. The estimates of T_{1F}^{-1} and T_{1S}^{-1} were obtained with fixed values $c_s = c_f = 0.5$ (for other fixed c_s and c_f values the T_{1F}^{-1} and T_{1S}^{-1} are slightly changed, but all features of the $T_{1F(S)}^{-1}(T)$ behavior discussed in paper remain).

The BPP model for describing the "dynamic" contribution to T_1^{-1}

The simplest model for describing the "dynamic" contribution to T_1^{-1} was proposed by Bloembergen, Purcell and Pound.[20] In the framework of this model, the exponential decay of the correlation function is assumed:

$$G(t) = \exp(-t/\tau_c). \quad (2)$$

In this case, the temperature dependence of T_1^{-1} is determined by an expression of the form

$$T_1^{-1}(T) = C\{J^{(1)}(\omega_0) + 4J^{(2)}(2\omega_0)\}, \quad (3)$$

$$J^{(n)}(\omega_0) = \frac{2\tau_c}{1+(n\omega_0\tau_c)^2}, \quad (4)$$

where C is determined by the nature of the interaction inducing the spin-lattice relaxation, for example, for the homonuclear dipolar interaction $C \sim \langle\Delta\omega_{II}^2\rangle$ (in the case of heteronuclear interaction, expression (3) is modified to take into account the *IS* contribution).[21] The $J^{(n)}(n\omega_0)$ –

is the spectral density function: the result of the Fourier transform of the correlation function $G(t)$. The τ_c is the correlation time, which in our case can be taken equal to the average residence time of the ion, $\tau_c = \tau_d$, which, in turn, is determined by the Arrhenius law:

$$\tau_d = \tau_{d0} \exp(E_a / k_B T). \quad (5)$$

Here k_B is the Boltzmann constant, and τ_{d0} is the average residence time of an ion at an infinite temperature (the value of τ_{d0}^{-1} is the so called "attempts frequency" coinciding in order of magnitude with the phonon frequency ~ 10^{11}–10^{14} s^{-1}). The BPP model assumes the appearance of a symmetrical maximum on the dependence $\ln T_1^{-1}$ vs. T^{-1}. The temperature of the T_1^{-1} maximum, T_{max}, corresponds to the temperature where the ion jump frequency becomes comparable with the resonance frequency: $\tau_d^{-1} \sim \omega_0$ (i.e. reaches the value of ~ 10^9 s^{-1} in our case). The high- and low-temperature slopes are equal to E_a/k_B and $-E_a/k_B$, respectively.

Pertaining the mechanisms determining the ^{23}Na spin-lattice relaxation in the $Na_9Al(MoO_4)_6$, we limited our further considerations to a purely quadrupole interaction. Indeed, our estimates of the ^{23}Na NMR line second moment value yield the $\langle \Delta\omega^2 \rangle \sim 10^7$ c^{-2}, which in turn gives a value $(T_1^{-1})_{max}$ not exceeding ~ 0.1 s^{-1}. This value is significantly lower than those experimentally observed (~ $5 \cdot 10^2$ s^{-1}). Thus, it is clear that the dipolar contribution to T_1^{-1} can be neglected. Quadrupolar spin-lattice relaxation also can be treated by means of Eq. (3) with

$$C = \frac{3}{40}\left(\frac{e^2 qQ}{\hbar}\right)^2\left(1+\frac{\eta^2}{3}\right) \quad (6)$$

Here, $e^2qQ/h \equiv C_Q = \{2I(2I–1)/3\}\nu_Q$ is the quadrupole coupling constant (QCC), η is the EFG asymmetry parameter (was equal to 0.4 in our case). It has to be noted that this approach has some significant restrictions. Strictly speaking, Eq. (3) is applicable only for nuclei with spin $I = 1$.[1] However, such an expression can be applied in the case of a spin system having a common spin temperature (i.e. when the $M_z(t)$ recovery is described by a single exponent) and it allows to obtain reasonable results for $I = 3/2$.[22–29] So, we also tried to use this expression as a rough approximation for the independent treatment of T_{1S}^{-1} and T_{1F}^{-1} components, assuming that it gives nevertheless a correct asymptotic behavior.

The "coupling model"

The main idea of "coupling model" proposed by Ngai [22, 30–34] is based on the assumption that at low temperatures the motion is slowing down due to the interaction of the diffusing ion with other ions. In this case, E_a^{NMR} is expected to be close to the real value of the energy barrier for the elementary jump, E_a, whereas E_a^{cond} is overestimated due to the correlation effects in ion motion.

As a result, the following relation should be fulfilled:

$$E_a = E_a^{NMR} = \beta E_a^{cond}. \quad (7)$$

In this case, the correlation function is described by the stretched exponential function:

$$G'(t) = \exp(-t/\tau_c)^{\beta}, \quad (8)$$

and Eqs. (5) and (4) for the spectral density function and spin-lattice relaxation rate are transformed into the form

$$J'^{(n)}(\omega_0) = \frac{2\tau_c}{1+(n\omega_0\tau_c)^{1+\beta}}, \quad (9)$$

$$T_1^{-1}(T) = C\{J'^{(1)}(\omega_0) + 4J'^{(2)}(2\omega_0)\}. \quad (10)$$

The coefficient $0 \le \beta \le 1$ indicates the presence of correlation effects in ionic motion: β = 1 corresponds to the case of "free" diffusion. The results of fitting the experimental data on T_{1S}^{-1} and T_{1F}^{-1} are shown in Figure 10 as black solid lines. The obtained parameters are E_a^{NMR} = 0.53±0.02 eV, β = 0.64±0.04, $\tau_{d0} \approx 3 - 4\cdot10^{13}$ s^{-1}, $\nu_Q \approx$ 130 and 190 kHz (for T_{1S}^{-1} и T_{1F}^{-1}, respectively). Finally, we tried to approximate the data on T_{1S}^{-1} and T_{1F}^{-1} simultaneously. In general case, the values of T_{1S}^{-1} and T_{1F}^{-1} are determined by more complicated ratios of the probabilities for quantum transitions Δm_I = 1 and Δm_I = 2 induced by both quadrupole and dipolar interactions.[35–37] Neglecting the dipolar contribution to T_1^{-1}, the expression for the spin-lattice relaxation rate can be reduced to the form:

$$T_{1S(F)}^{-1}(T) = C\left\{J'^{(1)}(\omega_0) + J'^{(2)}(2\omega_0) \pm \left[\left(J'^{(1)}(\omega_0) - J'^{(2)}(2\omega_0)\right)^2\right]^{1/2}\right\}, \quad (11)$$

which coincides with the predictions[38, 39], predicting $T_{1F}^{-1} \sim J^{(1)}(\omega_0)$ and $T_{1S}^{-1} \sim J^{(2)}(2\omega_0)$. The fit results of the experimental data on T_{1S}^{-1} and T_{1F}^{-1} by Eq. (11) are shown in Figure 10 as red solid lines. The parameter values are close to those obtained previously: E_a^{NMR} = 0.53±0.02 eV, β = 0.64 ±0.04, $\tau_{d0} \approx 3\cdot10^{13}$ s^{-1}, $\nu_Q \approx$ 150 kHz.

References

(1) Abragam, A. The Principles of Nuclear Magnetism. Clarendon Press: Oxford, UK, **1961**, 599 p.

(2) Man. P.P. Quadrupole Couplings in Nuclear Magnetic Resonance, General in Encyclopedia of Analytical Chemistry; R.A. Meyers (Ed.) John Wiley & Sons Ltd, Chichester, **2000**, 12224–12265.

(3) Massiot, D.; Fayon, F.; Capron, M.; King, I.; Le Calvé, S.; Alonso, B.; Durand, J.-O.; Bujoli, B.; Gan, Zh.; Hoatson, G. Modelling one- and two-dimensional solid-state NMR spectra. *Magn. Reson. Chem.* **2002**, *40*, 70–76.

(4) D. Massiot, R.; Conanec, W.; Feldmann, R.; Marchand, Y. NMR Characterization of the $Na_3AlP_3O_9N$ and $Na_2Mg_2P_3O_9N$ Nitridophosphates: Location of the $(NaAl)/Mg_2$ Substitution. *Inorg. Chem.* **1996**, .35, 4957–4960.

(5) Saitô, H.; Ando, I.; Ramamoorthy, A. The heart of NMR: Insights into biological aspects of proteins. *Progr. Nucl. Magn. Reson. Spectros.* **2010**, 57, 181–228.

(6) Grey, C. P., Dupré, N. NMR Studies of Cathode Materials for Lithium-Ion Rechargeable Batteries. *Chem. Rev.*, **2004,** 104, 4493–4512.

(7) Kim, N; Stebbins, J. F. $Sc_2(WO_4)_3$ and $Sc_2(MoO_4)_3$ and Their Solid Solutions: ^{45}Sc, ^{17}O, and ^{27}Al MAS NMR Results at Ambient and High Temperature. *Chem. Mater.* **2009**, 21, 309–315.

(8) Van Vleck, J. H. The Dipolar Broadening of Magnetic Resonance Lines in Crystals. *Phys. Rev.* **1948**, 74, 1168–1183.

(9) Hubbard, P.S. Nonexponential Nuclear Magnetic Relaxation by Quadrupole Interactions. *J. Chem. Phys.* **1970**, 53, 985–987.

(10) Van der Maarel, J. R. C. Thermal Relaxation and Coherence Dynamics of Spin 3/2. I. Static and Fluctuating Quadrupolar Interactions in the Multipole Basis. *Concepts. Magn. Reson. A* **2003**, 19A(2), 97–116.

(11) Groot, L. C. A.; Van der Maarel, J. R. C.; Leyte, J. C. 23Na Relaxation in Isotropic and Anisotropic Liquid-Crystalline DNA Solutions. *J. Phys. Chem.* **1994**, 98, 2699–2705.

(12) Bloise, A. C.; Donoso, J. P.; Magon, C. J.; Schneider, J.; Panepucci, H.; Benavente, E.; Sanchez, V.; Santa Ana, M. A.; González, G. NMR Study of Lithium Dynamics and Molecular Motions in a Diethylamine-Molybdenum Disulfide Intercalation Compound. *J. Phys. Chem. B* **2002**, 106, 11698–11707.

(13) Indris, S.; Heitjans, P. Heterogeneous ^7Li NMR relaxation in nanocrystalline $Li_2O:B_2O_3$ composites. *J. Non-Cryst. Solids* **2002**, 307–310, 555–564.

(14) Haaks, M.; Kaspar, J.; Franz, A.; Graczyk-Zajac, M.; Riedel, R.; Vogel, M. ^7Li NMR studies of lithium ion dynamics in polymer-derived silicon oxycarbide ceramics. *Solid State Ion.* **2016**, 287, 28–35.

(15) Wilkening, M.; Indris, S.; Heitjans, P. Heterogeneous lithium diffusion in nanocrystalline $Li_2O:Al_2O_3$ composites. *Phys. Chem. Chem. Phys.* **2003**, 5, 2225–2231.

(16) Emery, J.; Bohnke, O.; Florian, P.; Marzouk, K. NMR Study of Li^+ Ion Dynamics in the Perovskite $Li_{3x}La_{1/3-x}NbO_3$. *J. Phys. Chem. B* **2005**, 109, 20680–20689.

(17) Kelly, S. W.; Sholl, C. A. A relationship between nuclear spin relaxation in the laboratory and rotating frames for dipolar and quadrupolar relaxation. *J. Phys: Condens. Matter*. **1992**, 4, 3317–3330.

(18) Körblein, A.; Heitjans, P.; Stöckmann, H.-J.; Fujara, F.; Ackermann, H.; Buttler, W.; Dörr, K.; Grupp, H. Diffusion processes in solid Li-Mg and Li-Ag alloys and the spin-lattice relaxation of ^{8}Li. *J. Phys. F: Met. Phys.* **1985**, I5, 561–577.

(19) Stöckmann, H.-J.; Heitjans, P. Low-temperature nuclear spin-lattice relaxation in glasses – homogeneous and inhomogeneousous averaging. *J. Non-Cryst. Solids* **1984**, 66, 501–509.

(20) Bloembergen, N.; Purcell, E.M.; Pound, R.V. Relaxation Effects in Nuclear Magnetic Resonance Absorption. *Phys. Rev.* **1948**, 73, 679–715.

(21) Shinar, J.; Davidov, D.; Shaltiel, D. Proton NMR Study of Diffusion in Continuous, non Stoichiometrc Metal Hydrogen Systems HfV_2H_x and ZrV_2H_x. *Phys. Rev. B: Condens. Matter Mater. Phys.* **1984**, 30, 6331–6341.

(22) Arbi, K.; Tabellout, M.; Lazarraga, M. G.; Rojo, J. M.; Sanz, J. Non-Arrhenius conductivity in the fast lithium conductor $Li_{1.2}Ti_{1.8}Al_{0.2}(PO_4)_3$: A ^{7}Li NMR and electric impedance study. *Phys. Rev. B* **2005**, 72, 094302.

(23) Storek, M.; Böhmer, R.; Martin, S. W.; Larink, D.; Eckert, H. NMR and conductivity studies of the mixed glass former effect in lithium borophosphate glasses. *J. Chem. Phys.* **2012**, 137, 124507.

(24) Bloise, A. C.; Donoso, J. P.; Magon, C. J.; Schneider, J.; Panepucci, H.; Benavente, E.; Sanchez, V.; Santa Ana, M. A.; González, G. NMR Study of Lithium Dynamics and Molecular Motions in a Diethylamine-Molybdenum Disulfide Intercalation Compound. *J. Phys. Chem. B* **2002**, *106*, 11698–11707.

(25) Emery, J.; Bohnke, O.; Florian, P.; Marzouk K. NMR Study of Li^{+} Ion Dynamics in the Perovskite $Li_{3x}La_{1/3-x}NbO_3$. *J. Phys. Chem. B* **2005**, 109, 20680–20689.

(26) Kuhn, A.; Narayanan, S.; Spencer, L.; Goward, G.; Thangadurai, V.; Wilkening, M. Li self-diffusion in garnet-type $Li_7La_3Zr_2O_{12}$ as probed directly by diffusion-induced ^{7}Li spin-lattice relaxation NMR spectroscopy. *Phys. Rev. B* **2011**, 83, 094302.

(27) Kuhn, A.; Kunze, M.; Sreeraj, P.; Wiemhöfer, H.-D.; Thangadurai, V.; Wilkening, M.; Heitjans, P. NMR relaxometry as a versatile tool to study Li ion dynamics in potential battery materials. *Solid State Nuclear Magnetic Resonance* **2012**, 42, 2–8.

(28) Viefhaus, T.; Bolse, T.; Müller K. Oxygen ion dynamics in yttria-stabilized zirconia as evaluated by solid-state 17O NMR spectroscopy. *Solid State Ion.* **2006**, 177, 3063–3068.

(29) Sen, S.; Stebbins, J. F. Na-ion transport in borate and germanate glasses and liquids: A ^{23}Na and ^{11}B NMR spin-lattice-relaxation study. *Phys. Rev.* **1997**, 55, 3512–3519.

(30) Kanert, O.; Steinert, J.; Jain, H.; Ngai, K. L. Nuclear spin relaxation and atomic motion in inorganic glasses. *J. Non-Crystalline Solids* **1991**, 131–133, 1001–1010.

(31) Ngai, K. L.; Kanert, O. Comparison between the coupling model predictions, Monte Carlo simulations and some recent experimental data of conductivity relaxation in glassy ionics. *Solid State Ion.* **1992**, 53–56, 936–946.

(32) Ngai, K. L. Analysis of NMR and conductivity-relaxation measurements in glassy Li_2S-SiS_2 fast-ion conductors. *Phys. Rev. B* **1993**, 48, 13481–13485.

(33) Ngai, K. L.; Rizo, A. K. Parameterless Explanation of the Non-Arrhenius Conductivity in Glassy Fast Ionic Conductors. *Phys. Rev. Lett.* **1996**, 76, 1296–1299.

(34) Funke, K. Jump relaxation in solid electrolytes. *Prog. Solid St. Chem.* **1993**, 22, 111–195.

(35) Brinkmann, D.; Mali, M.; Roos, J.; Messer, R.; Birli, H. Diffusion processes in the superionic conductor Li_3N: An NMR study. *Phys. Rev. B* **1982**, 26, 4810–4825.

(36) Hughes, D. G. Non-exponential magnetic relaxation of I = 3/2 nuclear spins in solids. *J. Phys.: Condens. Matter*. **1993**, 5, 2025–2032.

(37) Yesinowski, J. P. Finding the true spin–lattice relaxation time for half-integral nuclei with non-zero quadrupole couplings. *J. Magn. Resonance* **2015**, 252, 135–144.

(38) Groot, L. C. A.; Van der Maarel, J. R. C.; Leyte, J. C. 23Na Relaxation in Isotropic and Anisotropic Liquid-Crystalline DNA Solutions. *J. Phys. Chem.* **1994**, 98, 2699–2705.

(39) Van der Maarel J.R.C. Relaxation of spin 3/2 in a nonzero average electric field gradient. *Chem. Phys. Lett*. **1989**, 155, 288–296.